energies

MDPI

Article

Low-Thermal-Budget Enhancement of Electrically Conductive Adhesive Interconnection for HPBC Photovoltaic Modules

Min Kwak [1,2], Woocheol Choi [1,2], Geonu Kim [1,3], Kiseok Jeon [1], Jinyong Seok [1], Jinho Shin [1,4] and Chaehwan Jeong [1,2,*]

[1] Energy & Nano Group, Korea Institute of Industrial Technology, Gwangju 61012, Republic of Korea; wg7012@kitech.re.kr (M.K.); bomfe0162@kitech.re.kr (W.C.); geonu@kitech.re.kr (G.K.); jks8287@kitech.re.kr (K.J.); sjwlsdyd@kitech.re.kr (J.S.); sjh5683@kitech.re.kr (J.S.)
[2] Department of Convergence Manufacturing System Engineering, University of Science and Technology, Daejeon 34113, Republic of Korea
[3] Department of Polymer Science and Engineering, Chonnam National University, Gwangju 61186, Republic of Korea
[4] Department of Materials Science and Engineering, Chonnam National University, Gwangju 61186, Republic of Korea
* Correspondence: chjeong@kitech.re.kr; Tel.: +82-62-600-6380

Abstract

The growing demand for high-efficiency photovoltaic (PV) technologies has intensified interest in advanced cell architectures, including hybrid passivated back contact (HPBC) solar cells. Conventional solder-based interconnection processes require high thermal budgets, which can induce thermomechanical stress and lead to performance degradation in thin back-contact cell structures. In this study, electrically conductive adhesive (ECA) interconnection is investigated as a low-thermal-budget, solder-free alternative for HPBC solar cells. The curing behavior of an acrylic-based, silver-filled ECA is systematically examined by controlling the upper lamp temperature and the welding time during the interconnection process. Electrical performance is evaluated through current–voltage characterization, fill factor, and series resistance analysis, while interfacial microstructural evolution is examined using scanning electron microscopy. The results identify a well-defined processing window in which adequate curing enables stable electrical contact formation. In contrast, both insufficient curing and excessive curing result in degraded electrical performance. To assess practical applicability, HPBC modules with an industry-relevant size of ~1000 × 1160 mm^2 are fabricated and evaluated using electroluminescence imaging and I–V measurements. By identifying a robust curing window and demonstrating its successful transfer from string-level interconnections to full-size HPBC modules, this study establishes a practical, low-thermal-budget, solder-free interconnection strategy for advanced back-contact PV architectures.

Keywords: hybrid passivated back contact (HPBC); electrically conductive adhesive (ECA); solder-free interconnection; HPBC photovoltaic; low-thermal-budget

Check for updates

Academic Editor: Carlo Renno

Received: 24 December 2025
Revised: 16 January 2026
Accepted: 19 January 2026
Published: 20 January 2026

Copyright: © 2026 by the authors. Licensee MDPI, Basel, Switzerland. This article is an open access article distributed under the terms and conditions of the Creative Commons Attribution (CC BY) license.

1. Introduction

Hybrid passivated back contact (HPBC) solar cells are widely recognized as one of the most promising crystalline silicon photovoltaic (PV) architectures for next-generation high-efficiency modules. By completely eliminating front-side metallization, HPBC designs maximize the effective light-absorbing area while enabling advanced surface and

interface passivation for both charge carrier polarities. Owing to these structural advantages, certified power conversion efficiencies exceeding 26% at the cell level and more than 24% at the module level have been reported. These results position HPBC technology among the highest-performing PV architectures compatible with industrial manufacturing processes [1–3].

Despite these achievements, a persistent performance gap remains between cell-level efficiency and the efficiency realized at the module level. This discrepancy is largely attributed to cell-to-module (CTM) losses introduced during cell cutting, handling, and interconnection. Among these loss mechanisms, interconnection-induced series resistance (R_s) is particularly critical, as it directly degrades the fill factor (FF) and limits output power [4,5]. This effect is especially pronounced in HPBC architectures, where current collection relies exclusively on rear-side metallization. As a result, HPBC modules are highly sensitive to local contact degradation and non-uniform interconnection quality [6,7].

The importance of interconnection reliability has further increased with the transition toward larger cell formats, such as M10 and G12, combined with the continued reduction of wafer thickness to below 120 μm. Conventional solder-based interconnection processes typically require high-temperature reflow exceeding 200 °C. Such conditions introduce substantial thermomechanical stress and increase the risk of wafer bowing, microcrack formation, metallization delamination, and long-term reliability degradation under thermal cycling and damp-heat exposure [8–10].

Electrically conductive adhesives (ECAs) have therefore emerged as a promising solder-free alternative, offering reduced thermal budgets and improved mechanical compliance [11–14]. However, the electrical performance of ECA-based interconnections is highly sensitive to curing conditions. Insufficient curing results in incomplete conductive network formation, whereas excessive curing can induce microstructural degradation within the adhesive. Both effects increase R_s and degrade the FF [15]. These competing mechanisms define a narrow processing window for achieving optimal electrical performance.

Previous studies on ECA curing have primarily focused on isothermal or quasi-isothermal conditions and on conventional cell architectures [16,17]. In parallel, ECA interconnection has been extensively investigated in shingled module concepts, with emphasis on localized bonding strategies and mechanical reliability [18,19]. More recently, low-temperature interconnection approaches have been explored for emerging PV technologies, including perovskite–silicon tandem cells and material-efficient module designs. These studies highlight the growing importance of precise thermal control under reduced thermal budgets [20–22].

In contrast, HPBC interconnection imposes additional constraints that are not adequately captured by isothermal curing frameworks. Due to the rear-contact-only configuration, HPBC cells exhibit limited tolerance to local contact degradation. Furthermore, recent interconnection schemes increasingly rely on localized and transient heating methods. These approaches inherently involve strongly non-isothermal, spatially non-uniform, and transient thermal conditions [23].

Among these methods, lamp-assisted localized heating offers a distinct advantage by concentrating thermal input near the interconnection interface. This approach promotes solvent evaporation and polymer crosslinking while minimizing excessive heating of the bulk silicon wafer. Under such conditions, however, the true interfacial temperature is inherently ill-defined and cannot be reliably reconstructed using conventional thermocouples or infrared thermography, particularly on millisecond time scales. As a result, direct application of conventional curing kinetics models or absolute temperature-based criteria becomes impractical, despite their validity under strictly isothermal conditions [16,17].

In this study, the lamp set temperature and welding time are therefore adopted as process-controllable parameters, rather than attempting to infer the actual interfacial temperature history. To enable systematic interpretation of experimental results obtained under different temperature–time combinations, a semi-empirical quadratic thermal exposure (QTE) parameter is introduced as an interpretive coordinate. The QTE parameter is not intended to serve as a predictive kinetic model or a material-specific constant. Instead, it provides a normalized framework for organizing curing conditions under non-isothermal processing environments.

The present work focuses on the formative stage of ECA-based interconnection, examining the relationship between processing conditions and electrical response at both the string and module levels. Electrical performance is evaluated through I–V characterization, FF analysis, R_s extraction, and electroluminescence (EL) imaging. Interfacial microstructural evolution is examined using scanning electron microscopy. In addition, full-size HPBC modules with industry-relevant dimensions of ~1000 × 1160 mm^2 are fabricated to assess process transferability and curing uniformity under realistic manufacturing constraints. By identifying an optimized curing window under non-isothermal conditions and demonstrating scalability from string-level interconnections to full-size modules, this work establishes a low-thermal-budget, solder-free interconnection strategy tailored to advanced HPBC PV technologies.

2. Materials and Methods

2.1. HPBC Cell Interconnection and Lamp-Assisted Welding Process

Figure 1 presents a schematic comparison between conventional solder-based interconnection and the ECA-based interconnection approach employed in this study. Conventional soldering typically requires localized application of high temperatures exceeding 250 °C to form metallurgical joints. Such processes can induce thermal damage to the solar cells and require the use of flux as well as lead-containing solder materials. In contrast, lamp-assisted ECA interconnection enables bonding at substantially lower surface temperatures by combining polymer-based conductive adhesives with localized radiative heating. This approach reduces thermomechanical stress and enables both lead-free and flux-free processing.

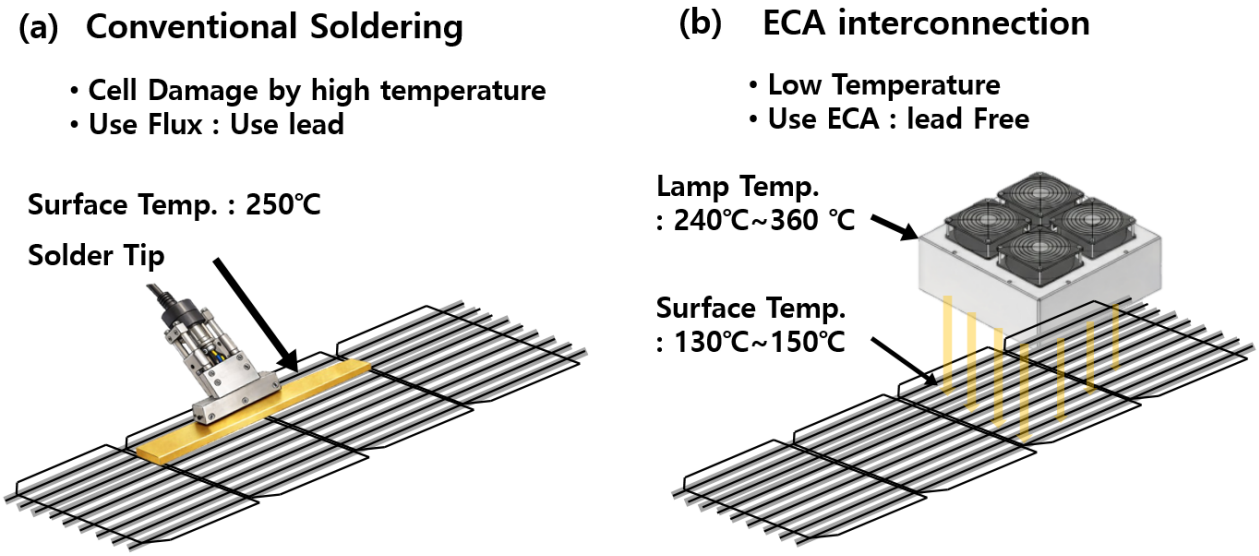


Figure 1. Comparison between conventional soldering and ECA interconnection.

Commercial-grade HPBC crystalline silicon solar cells were first cut into half-cell configurations. Twelve half-cut cells were then serially interconnected using Sn–Pb ribbons

with dimensions of 0.7 mm × 0.15 mm to form a single string, as schematically illustrated in Figure 2a. For electrical characterization, the fabricated string was subsequently segmented into two-cell units by cutting at predefined locations. For module-level interconnection, wider Sn–Pb ribbons with dimensions of 6 mm × 0.35 mm were employed to reflect industry-relevant configurations.

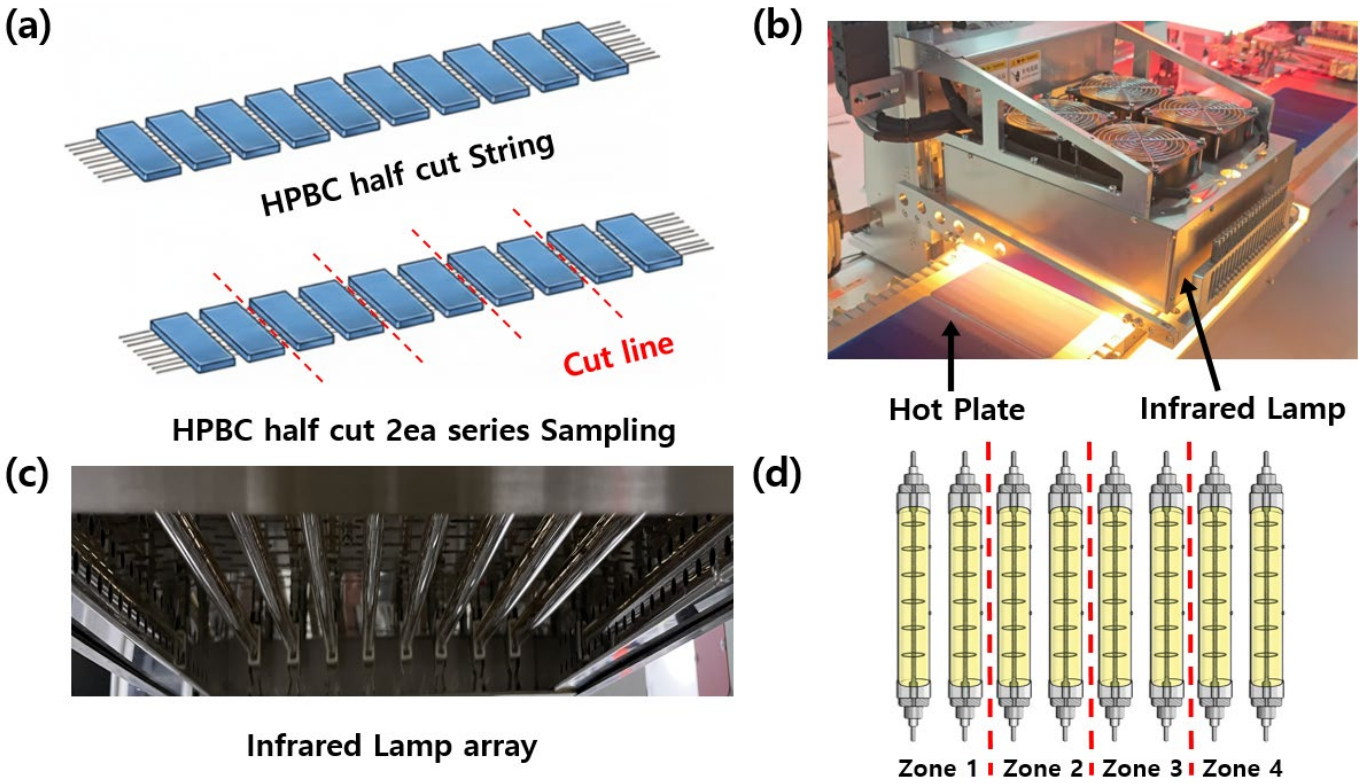


Figure 2. (**a**) Fabrication process of HPBC half-cut cell string. (**b**) Photograph of lamp-assisted welding system. (**c**) Photograph of the infrared lamp array. (**d**) Lamp zone schematic.

Interconnection was performed using a combined plate-heating and lamp-assisted welding process. A photograph of the lamp-assisted light box system used in this study is shown in Figure 2b. The plate heater provided a constant baseline temperature across the cells, while localized thermal energy was delivered to the cell–ribbon–ECA region through infrared lamp-assisted welding.

The lamp-assisted heating was provided by tungsten-filament infrared lamps enclosed in fused-silica quartz tubes (99.9% purity). The heating system was configured with four independently controlled zones, each consisting of two infrared lamps, allowing spatially distributed and controllable radiative heating during interconnection. A photograph of the infrared lamp array employed in this study is shown in Figure 2c, while the corresponding lamp zone configuration is illustrated schematically in Figure 2d.

The lamps emit predominantly in the near-infrared range (peak wavelength: 0.75–1.4 μm) with a rapid thermal response of approximately 1 s, enabling highly localized and transient heating at the interconnection region. Owing to the high filament temperature (1800–2400 °C) and the radiative nature of heat transfer, the delivered thermal input is governed primarily by the lamp output setting rather than by a well-defined steady-state surface temperature.

The key lamp heating parameter in this study, hereafter referred to as the upper lamp temperature, denotes the set temperature of the lamp heating source rather than the actual surface or interfacial temperature of the solar cell. The upper lamp temperature values reported herein were obtained by directly measuring the lamp surface temperature using

an infrared thermometer under steady-state lamp operation. It should be emphasized that this measured lamp surface temperature does not represent the temperature at the cell–ribbon–ECA interface, but serves as a reproducible reference parameter reflecting the relative radiant thermal output of the lamp.

To verify the spatial reproducibility of the lamp-assisted heating, the relative surface temperature beneath the infrared lamp was measured at nine discrete locations (4 × 1 grid) under steady-state operation, as shown in Figure 3. No pronounced hot spots or steep spatial gradients were observed across the effective heating area, indicating spatially consistent radiative output under the present configuration.

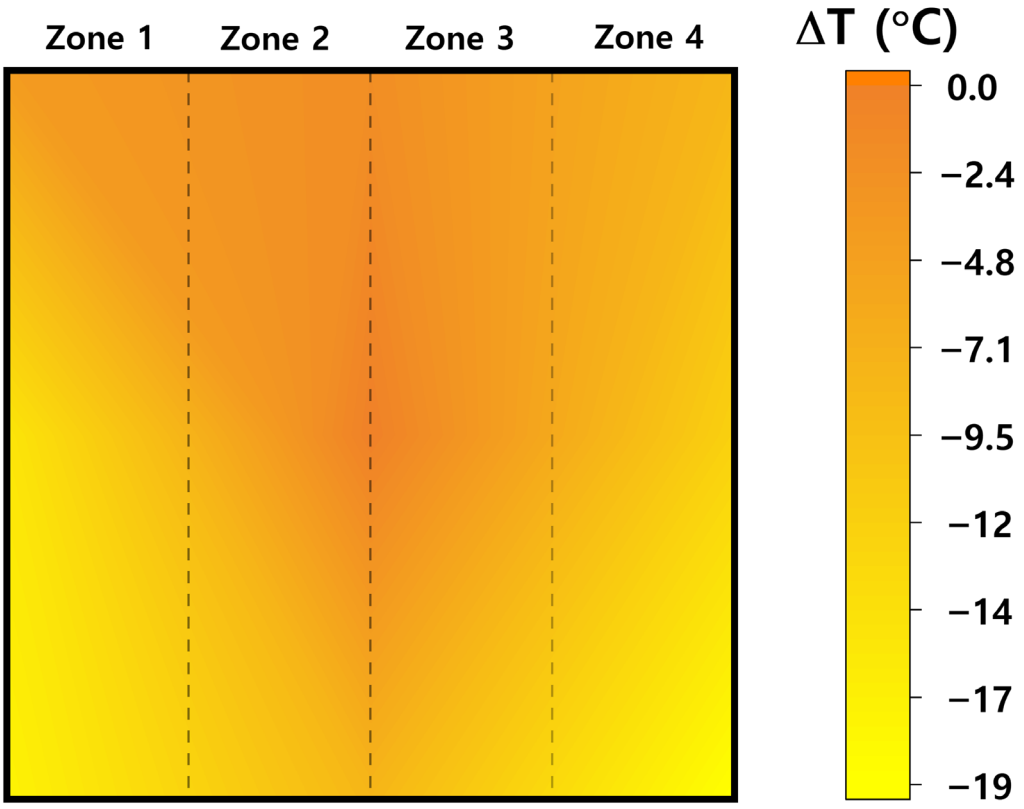


Figure 3. Relative surface temperature map beneath the infrared lamp, constructed from measurements on a 4 × 1 grid under steady-state conditions.

Because the actual interfacial temperature at the cell–ribbon–ECA junction cannot be directly measured under lamp-assisted welding conditions, the upper lamp temperature was adopted as a practical and process-controllable parameter for comparing the relative thermal input delivered under different welding conditions. Throughout this study, the plate temperature was maintained at a constant value of 130 °C. All other processing parameters, including applied pressure and ambient conditions, were held constant, while only the lamp-assisted heating parameters, namely the upper lamp temperature and the welding time ranging from 1 to 5 s, were systematically varied.

2.2. Characterization Methods

The electrical performance of the interconnected samples was evaluated using a solar simulator (XHS-4040B300KPV1, Seric Co., Koshigaya, Japan) under standard test conditions (STC). These conditions correspond to an irradiance of 1000 $W \cdot m^{-2}$, a cell temperature of 25 °C, and an AM 1.5G spectral distribution. Current–voltage (I–V) characteristics were measured using an IV tracer (DKSCT-100-200, Denken Co., Tokyo, Japan). From the

measured I–V curves, key PV parameters were extracted, including open-circuit voltage (V_{oc}), short-circuit current (I_{sc}), FF, conversion efficiency, and R_s.

For each processing condition, at least three independent samples were fabricated and characterized. The reported values represent the average of these measurements.

Microstructural characterization was performed using scanning electron microscopy (SEM, SNE-4500M, SEC Co., Ltd., Suwon, Republic of Korea) to qualitatively examine interfacial morphology and microstructural features associated with ECA curing at the cell–ribbon interface. Both surface and cross-sectional morphologies were analyzed to identify curing-related morphological differences. SEM observations were used solely for qualitative assessment and were not employed for quantitative evaluation or direct determination of the curing state.

2.3. HPBC Module Fabrication and Evaluation

To evaluate the scalability of the optimized ECA curing conditions, a full-size HPBC solar module with an industry-relevant area of ~1000 × 1160 mm^2 was fabricated. The module was assembled using HPBC half-cut cells interconnected by Sn–Pb ribbons and the same acrylic-based, silver-filled ECA. The interconnection process employed identical plate-heating and lamp-assisted welding conditions to those optimized at the string level.

The module array configuration was designed to reflect a conventional HPBC module layout, in which multiple ECA-bonded cell strings were electrically connected in series to achieve the target module voltage while minimizing additional resistive losses. A schematic illustration of the module array and cross-sectional configuration is shown in Figure 4. The module consists of 30 HPBC half-cut cells connected in series, with two such strings connected in parallel. After fabrication, the module was characterized using EL imaging to assess the uniformity of electrical activity and to identify interconnection-related defects. In addition, I–V characteristics of the fabricated module were measured under standard test conditions to verify overall electrical functionality and consistency with trends observed at the string level.

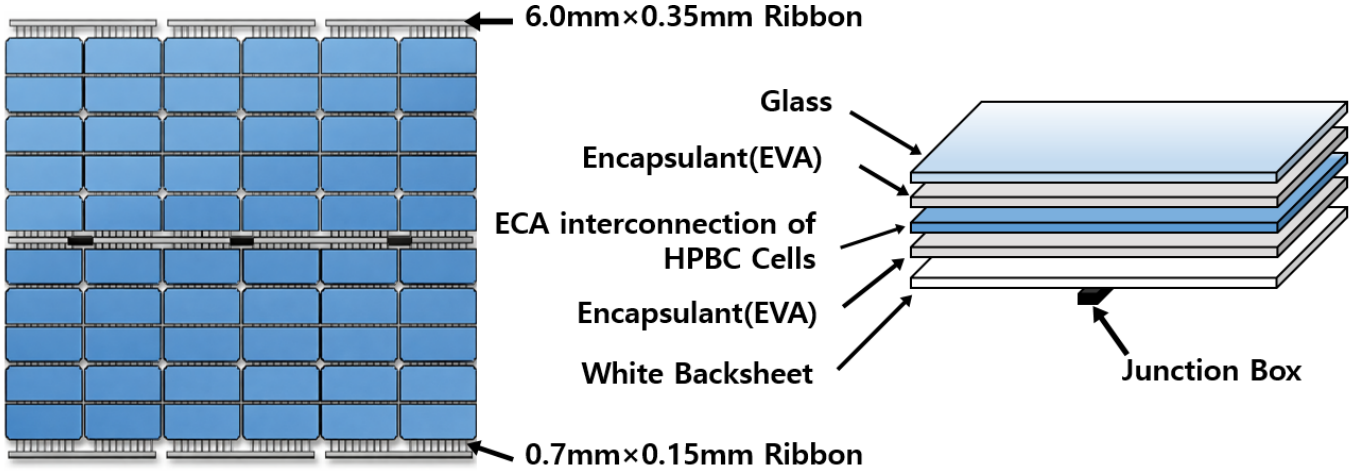


Figure 4. HPBC module array and cross-sectional schematic. Module configuration consists of 30 HPBC half-cut cells connected in series, with two strings connected in parallel.

3. Results and Discussion

3.1. Electrical Performance and Identification of the Optimized Curing Window

Interconnection experiments were systematically conducted by independently varying the upper lamp temperature and the welding time in order to investigate their combined effects on ECA curing behavior, interfacial contact formation, and electrical performance.

All other processing parameters, including applied pressure and ambient conditions, were held constant.

Figure 5 presents a process feasibility map for HPBC string fabrication as a function of upper lamp temperature and welding time. Fabrication outcomes were categorized as failed, stable, or unstable based on the mechanical integrity of the bonded ribbons and the electrical continuity of the fabricated strings

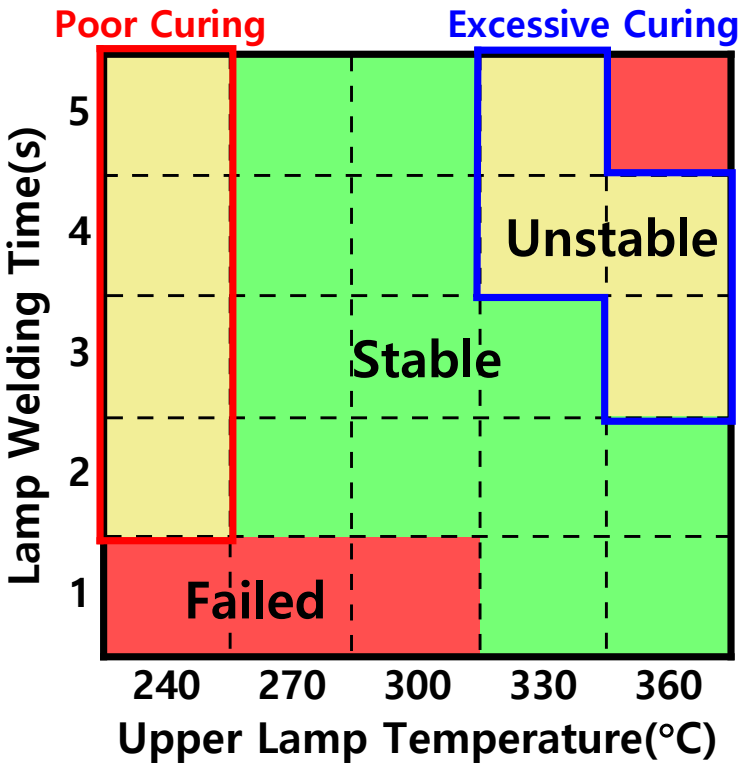


Figure 5. Process window for HPBC string fabrication defined by upper lamp temperature and lamp welding time. Fabrication feasibility is categorized as failed, stable, or unstable based on mechanical integrity and electrical continuity of the fabricated strings.

A distinct stable region is observed at intermediate lamp temperatures and moderate welding times, corresponding to a balanced thermal input that enables reliable ECA curing. In contrast, insufficient thermal input at lower temperatures or shorter welding times resulted in failed interconnections, while excessive thermal input at higher temperatures and longer welding times led to unstable bonding and performance degradation.

As shown in Figure 6, the conversion efficiency exhibits a clear non-monotonic dependence on the combined variation of upper lamp temperature and welding time. Under low-temperature or short-duration conditions, such as 240 °C for 2 s, the efficiency remains relatively low, indicating insufficient interconnection quality. In contrast, the highest efficiencies are consistently achieved within an intermediate temperature range of ~270 to 300 °C when moderate welding times are applied. These conditions define a well-defined optimized curing window. At higher temperatures combined with longer welding times, such as 330 to 360 °C with 4 to 5 s, a pronounced degradation in efficiency is observed. This degradation reflects performance losses induced by excessive thermal exposure and excessive curing of the ECA. The corresponding electrical parameters, including conversion efficiency, FF, and R_s, for all curing conditions are summarized in Table 1. Collectively, these results demonstrate that the electrical performance of HPBC interconnections under lamp-assisted curing is strongly governed by the combined thermal exposure arising from temperature–time coupling rather than by either parameter alone.

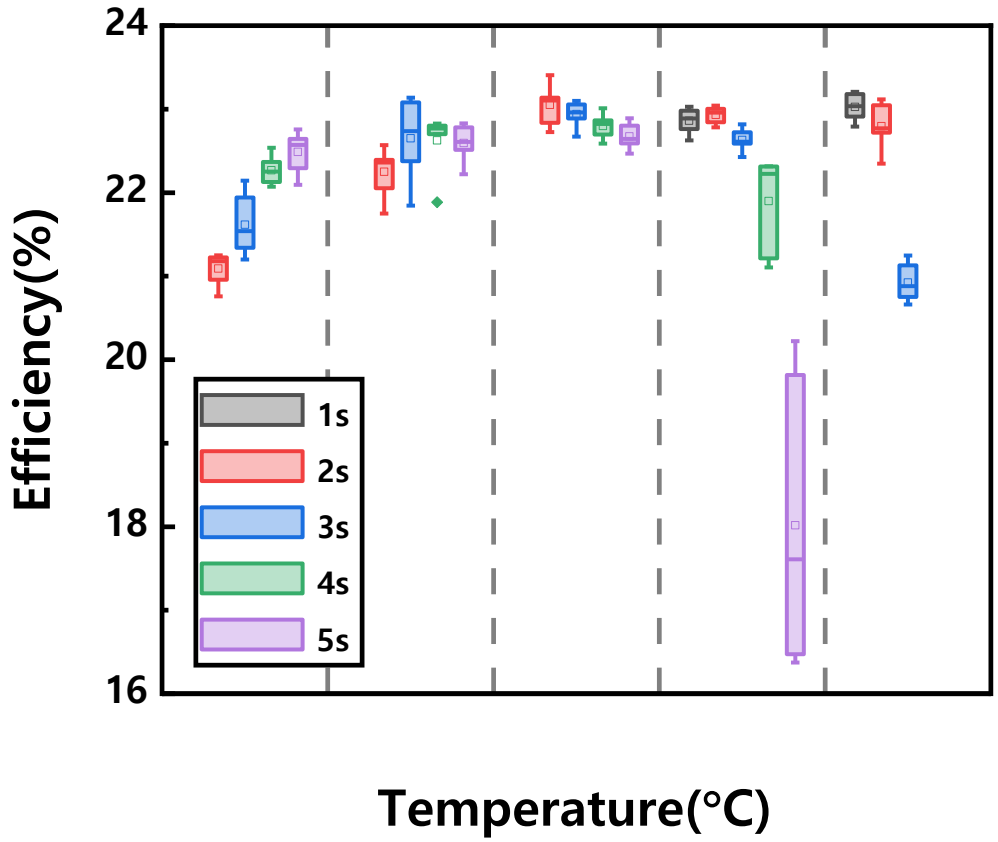


Figure 6. Conversion efficiency of HPBC half-cut two-cell series samples as a function of welding time from 1 to 5 s at different upper lamp temperatures ranging from 240 to 360 °C.

Table 1. Electrical characteristics of HPBC half-cut two-cell series samples under various curing conditions. A dash indicates fabrication failure.

Upper Lamp Temperature		Welding Time				
		1 s	**2 s**	**3 s**	**4 s**	**5 s**
240 °C	Efficiency (%)	-	21.0909	21.6170	22.2684	22.4884
	Fill Factor (%)	-	71.7201	73.1192	74.6118	74.7709
	R_s (mΩ)	-	24.1116	23.3138	22.3777	22.1568
270 °C	Efficiency (%)	-	22.2495	22.6519	22.6255	22.5937
	Fill Factor (%)	-	75.9865	76.6715	77.1133	76.3877
	R_s (mΩ)	-	21.3743	21.1874	21.0894	21.5748
300 °C	Efficiency (%)	-	23.0525	22.9399	22.7970	22.6736
	Fill Factor (%)	-	78.1264	77.1028	76.6764	77.1575
	R_s (mΩ)	-	19.5520	20.8104	21.4700	21.2501
330 °C	Efficiency (%)	22.8624	22.9320	22.6294	21.8991	18.0178
	Fill Factor (%)	77.2441	77.4922	77.1155	74.5296	63.5814
	R_s (mΩ)	21.3919	21.3017	21.3037	22.5320	29.5306
360 °C	Efficiency (%)	23.0276	22.7953	20.9246	11.2066	-
	Fill Factor (%)	77.1413	76.6431	72.7808	57.6407	-
	R_s (mΩ)	20.9199	21.1416	23.7334	40.1984	-

For comparison, a conventionally soldered interconnection was prepared and evaluated alongside the optimized ECA interconnection condition. Figure 7 shows the corresponding I–V characteristics, and the extracted electrical parameters are summarized in Table 2. Under the present experimental conditions, the optimized ECA interconnection

exhibits a slightly higher conversion efficiency and FF than the soldered reference while maintaining a comparable R_s. These results indicate that, despite the absence of metallurgical bonding, the optimized lamp-assisted ECA interconnection can achieve electrical performance comparable to, and in this case marginally exceeding, that of conventional soldering. The observed performance difference between the two interconnection approaches is modest, underscoring that the proposed lamp-assisted ECA process enables high electrical performance while operating under a substantially reduced thermal budget. This outcome highlights the potential of ECA-based interconnection as a viable solder-free alternative for HPBC solar cell modules.

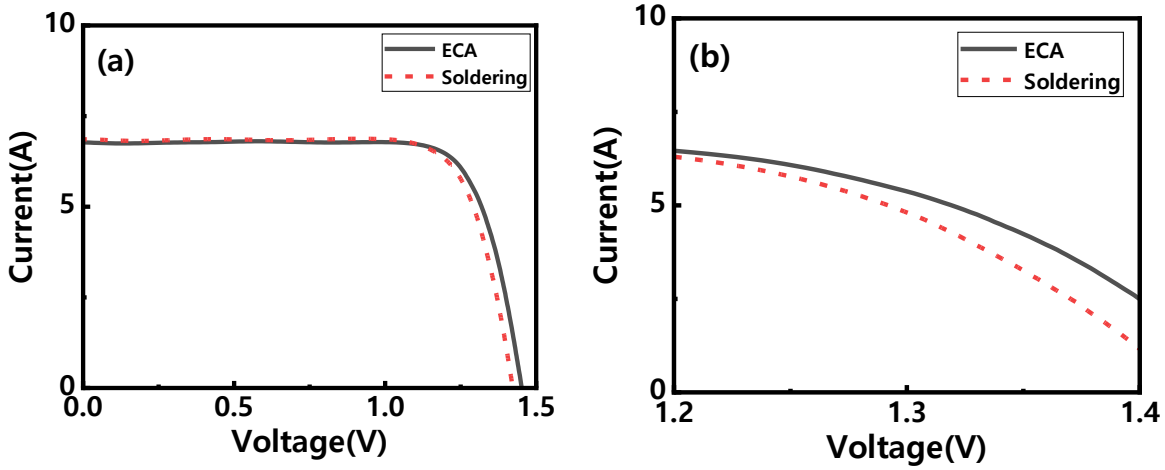


Figure 7. I–V characteristics of the optimized ECA interconnection and conventional soldering: (**a**) full I–V curves and (**b**) enlarged view near the maximum power point, highlighting differences in the knee region.

Table 2. Electrical comparison between optimized ECA interconnection and conventional soldering.

Interconnection	Efficiency (%)	Fill Factor (%)	R_s (mΩ)
ECA (Optimized)	23.0525	78.1264	19.5520
Soldering	22.9075	77.7871	18.9462

3.2. Morphological and Electroluminescence Correlation with Curing Regions

To qualitatively examine the microstructural features associated with the observed electrical behavior, SEM analysis was performed at the ECA–ribbon interface under representative curing conditions, as shown in Figure 8. Poorly cured samples are characterized by localized aggregation of silver fillers and a heterogeneous interfacial morphology. In contrast, samples processed within the optimized curing window exhibit a comparatively uniform interface without pronounced structural defects. In the excessively cured regime, microstructural degradation is observed in the form of pore formation and increased porosity. Such features are known to adversely affect electrical continuity and charge transport within conductive adhesive systems [24].

These microstructural observations indicate that the curing condition directly governs the formation, connectivity, and stability of the conductive filler network at the ECA–ribbon interface. This evolution is expected to manifest primarily as changes in R_s, which therefore serves as a sensitive electrical indicator linking curing-induced morphological changes to macroscopic device performance. This relationship is quantitatively reflected in the extracted R_s values summarized in Table 1, where both poorly cured and excessively cured conditions exhibit systematically higher R_s than samples processed within the optimized curing window.

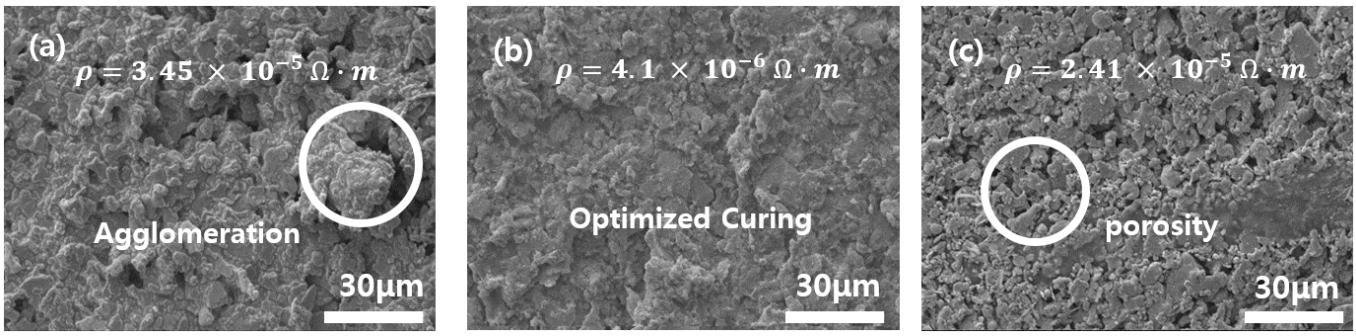


Figure 8. SEM images of ECA morphology under different curing conditions: (**a**) poor curing, (**b**) optimized curing, and (**c**) excessive curing.

Although SEM analysis provides valuable insight into interfacial morphology and filler network evolution, morphological observations alone cannot unambiguously determine the curing state of the ECA. Previous studies have shown that variations in filler loading and silver content can significantly influence contact resistivity and its stability in ECA-based interconnects, underscoring the necessity of electrical characterization beyond purely morphological assessment [25,26]. Consequently, the electrical implications of the observed microstructural differences are further examined through R_s trends, EL imaging, and I–V characterization, as discussed below.

The morphological features identified by SEM are further reflected in the electroluminescence imaging results summarized in Figure 9. Poorly cured samples exhibit pronounced non-uniform emission and localized dark regions along the ribbon paths, indicating incomplete current injection and non-uniform electrical contact formation. Samples processed within the optimized curing window show uniform EL emission across the active area, reflecting homogeneous and stable electrical contacts. In contrast, excessively cured samples display localized emission degradation and line-shaped intensity variations near the interconnection regions. These features are consistent with increased R_s and associated FF losses [27–29]. Thus, EL imaging provides spatially resolved evidence that supports the R_s trends inferred from the microstructural observations.

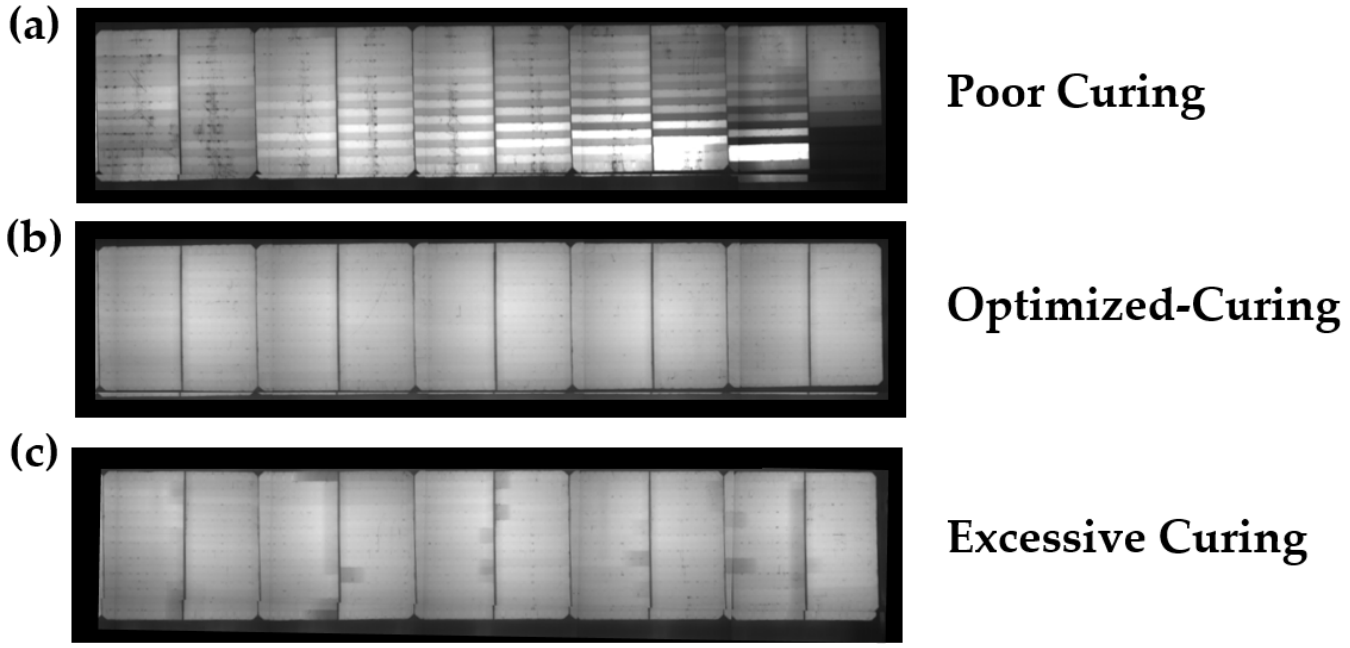


Figure 9. Electroluminescence (EL) images of HPBC strings under different curing regimes: (**a**) poor curing, (**b**) optimized curing, and (**c**) excessive curing.

Consistent trends are also observed in the measured I–V characteristics shown in Figure 10. Poorly cured samples exhibit a reduced slope near the maximum power point, indicating inefficient current collection and pronounced resistive losses. The resulting distortion of the I–V curve suggests non-ideal charge transport due to insufficient electrical contact formation. In contrast, optimally cured samples display a well-defined, rectangular I–V profile with a steep slope and a clearly defined maximum power point, demonstrating efficient charge transport and low-resistance interconnections. Excessively cured samples show degradation in I–V curvature, characterized by a flattened slope and reduced maximum power output relative to the optimized condition. This behavior is consistent with increased resistive losses and localized contact degradation [30,31]. These curing-dependent I–V characteristics are in good agreement with the trends in R_s inferred from the SEM and EL analyses, indicating that microstructural changes at the ECA–ribbon interface directly translate into macroscopic electrical performance variations.

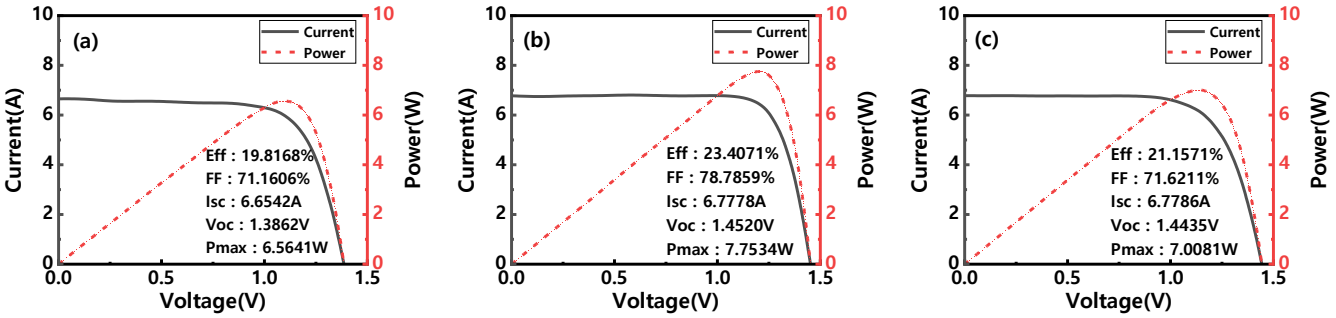


Figure 10. I–V characteristics of HPBC samples under different curing regimes: (**a**) poor curing, (**b**) optimized curing, and (**c**) excessive curing.

Overall, the evolution of the I–V curves demonstrates that optimized curing enables efficient charge transport, whereas both poor curing and excessive curing introduce morphology-related resistive limitations that degrade electrical performance.

3.3. Thermal-Exposure-Based Interpretation of ECA Curing Behavior

To rationalize the combined influence of upper lamp temperature and welding time under localized, non-isothermal curing conditions, a thermal-exposure-based interpretive framework was adopted as a post-processing approach. In lamp-assisted interconnection, the interfacial temperature history at the ECA–cell–ribbon junction is inherently transient, spatially non-uniform, and experimentally inaccessible. As a result, a simplified parameterization is required to systematically organize the experimentally observed trends obtained under different temperature–time combinations.

The curing behavior of polymer-based ECAs is generally understood as a thermally activated process and is commonly described using Arrhenius-type relations under isothermal conditions [16,17]. However, in the combined plate-heating and lamp-assisted configuration employed in this study, the curing environment deviates substantially from isothermal assumptions. Local temperatures vary rapidly due to localized lamp heating superimposed on a constant plate temperature, and the effective curing behavior is influenced not only by intrinsic chemical reaction kinetics but also by diffusion-limited processes, including polymer chain mobility, solvent evaporation, and conductive filler rearrangement [32]. Under these conditions, direct application of conventional kinetic models or absolute temperature-based curing criteria is not feasible.

Rather than attempting to reconstruct an ill-defined interfacial temperature history, the lamp set temperature is adopted as a process-controllable parameter that governs the relative thermal input delivered to the interconnection region. Under fixed geometric condi-

tions and exposure times, the lamp output setting provides a monotonic and reproducible proxy for the radiant energy supplied to the joint. On this basis, a semi-empirical QTE parameter is introduced as an interpretive metric. The QTE is not intended to function as a predictive curing-kinetics model or as a material-specific physical constant, but rather as a normalized framework for organizing experimental data obtained under non-isothermal processing conditions.

The QTE is formulated to reflect the strong non-linear sensitivity of polymer crosslinking and solvent removal processes to temperature within the experimentally relevant high-temperature regime, while retaining a simple functional form suitable for practical interpretation. Specifically, the effective thermal exposure during lamp-assisted curing is approximated by a quadratic dependence on the temperature difference relative to the plate temperature, leading to the following definition:

$$\mathrm{QTE} = \mathrm{t}\left(T_u - T_{plate}\right)^2, \tag{1}$$

where t is the welding time and T_u is the upper lamp temperature achieved during lamp-assisted heating, and T_{plate} is the constant plate temperature. This formulation does not represent reaction kinetics or the degree of cure, but instead serves as a relative measure of effective thermal exposure under localized heating conditions.

Among the measured electrical parameters, R_s was selected as the primary indicator for assessing the effectiveness of the QTE-based scaling. This choice is motivated by the direct sensitivity of R_s to the formation and stability of the silver filler network and to interfacial contact development in ECA-based joints, making it a reliable probe of curing quality under different processing conditions [33,34].

To enable qualitative comparison with the manufacturer-recommended curing condition for the ECA, namely 150 °C for 10 to 15 s under uniform heating, the QTE was further normalized into an equivalent curing time, t_{eq}, defined as:

$$t_{eq} = \frac{t(T_u - T_{Plate})^2}{K\left(T_{ref} - T_{Plate}\right)^2}, \tag{2}$$

where T_{ref} = 150 °C, T_{plate} = 130 °C, and K is a proportionality factor introduced solely to normalize the relative thermal-exposure scale to the reference curing condition. Importantly, K does not represent a physical constant. Variations in K result only in uniform rescaling of the t_{eq} axis and do not affect the relative ordering of data points or the position of the optimized curing window.

When the extracted R_s values are plotted as a function of the equivalent curing time t_{eq}, as shown in Figure 11 and Table 3, data obtained under different lamp temperature and welding time combinations collapse onto a common trend that exhibits a characteristic U-shaped dependence [23]. This collapse demonstrates that relative thermal exposure, rather than individual process parameters alone, governs ECA contact formation under localized heating conditions.

The R_s exhibits a clear U-shaped dependence on the t_{eq}, serving as a sensitive indicator of the ECA curing state. Based on the evolution of R_s, three distinct curing regimes can be identified: poor curing (t_{eq} < 10 s), optimized curing (10 s $\leq t_{eq} \leq$ 15 s), and excessive curing (t_{eq} > 15 s). The minimum observed at $t_{eq} \approx$ 12 to 13 s corresponds to a critical thermal-exposure window in which electrical performance is maximized. This regime is consistent with effective polymer crosslinking and conductive network formation without evidence of thermally induced degradation. Within this interpretive framework, QTE-

based scaling provides a unified and physically intuitive means of organizing experimental results obtained under diverse temperature–time processing conditions.

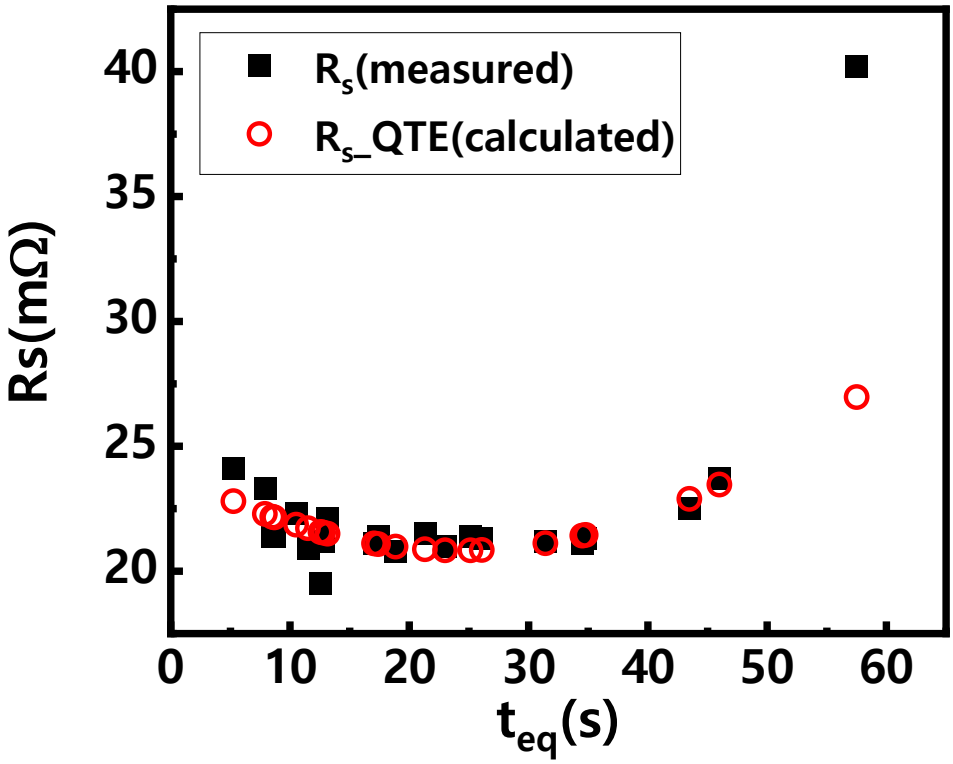


Figure 11. Comparison of experimentally measured electrical performance with QTE-based trends as a function of equivalent curing time t_{eq}.

Table 3. Summary of the equivalent curing times calculated for all experimental conditions.

Lamp Welding Time	Upper Lamp Temperature				
	240 °C	270 °C	300 °C	330 °C	360 °C
1 s	2.6	4.2	6.2	8.7	11.4
2 s	5.2	8.5	12.5	17.3	22.9
3 s	7.8	12.7	18.7	26.0	34.3
4 s	10.4	17.0	24.9	34.6	45.7
5 s	13.1	21.2	31.1	43.3	57.2

3.4. Module-Scale Demonstration of Localized ECA Curing

To demonstrate the practical applicability of the optimized curing conditions, a full-size HPBC module was fabricated using the same lamp-assisted ECA interconnection process optimized at the string level. Figure 12 presents a photograph and the corresponding electroluminescence image of the fabricated module. Uniform EL emission is observed across the active area, with no pronounced dark regions or interconnection-related defects. This behavior indicates homogeneous current injection and stable electrical contact formation throughout the module [4,29].

The measured I–V characteristics exhibit smooth diode behavior without abnormal curvature indicative of excessive R_s. The extracted electrical parameters are consistent with trends observed at the string level, confirming that the identified optimized curing window can be successfully transferred from small-scale interconnections to an industry-relevant module configuration [2,18]. Although the module-level results are presented as

a demonstration of feasibility rather than a statistical reliability assessment, they provide direct experimental evidence that localized, low-thermal-budget ECA curing is compatible with HPBC module fabrication.

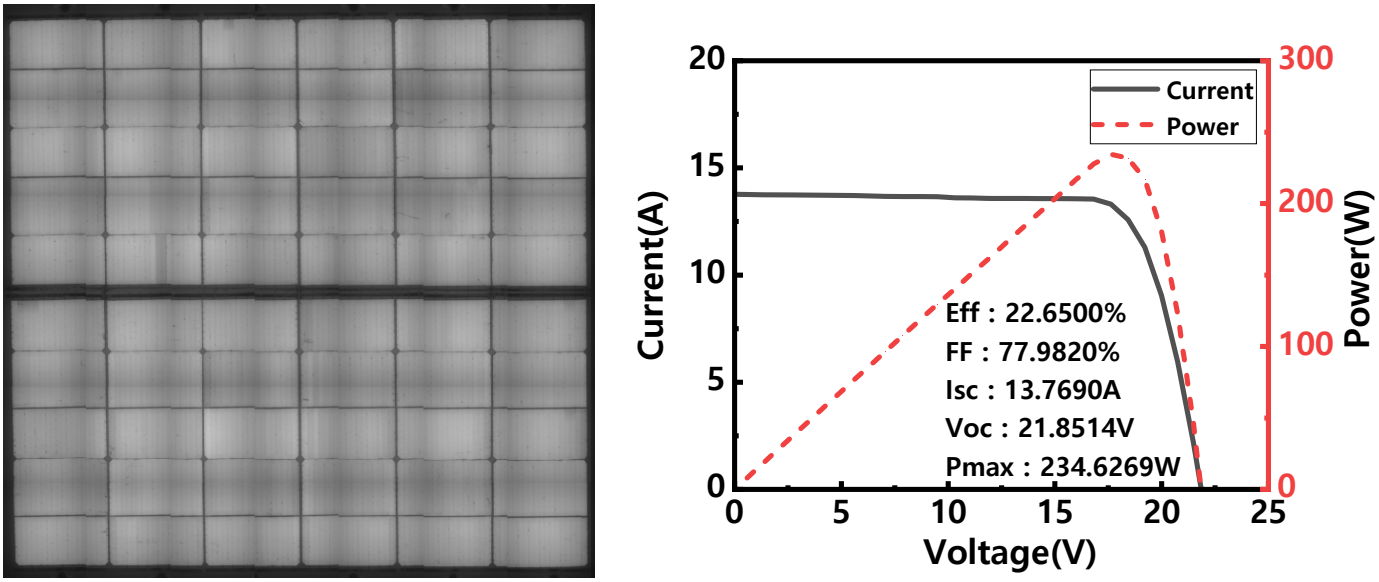


Figure 12. I–V characteristics and electroluminescence images of the fabricated HPBC module.

4. Conclusions

In this study, a localized rapid curing process for ECAs was systematically investigated and applied to industrial-scale HPBC solar cell modules. By correlating curing conditions with electrical performance, EL imaging, and module-level characteristics, three distinct curing regimes were clearly identified: poor curing, optimized curing, and excessive curing. The optimized curing window, corresponding to an equivalent curing time of ~10 to 15 s, yielded the lowest R_s and the highest module efficiency.

Within the optimized curing regime, stable electrical performance and relatively uniform current distribution were achieved without inducing excessive thermal damage. In contrast, insufficient curing resulted in incomplete electrical contact formation and degraded device performance, whereas excessive thermal input led to increased R_s accompanied by pronounced EL non-uniformity.

Importantly, the proposed localized curing approach demonstrated strong applicability to large-area HPBC modules, enabling uniform ECA curing across the entire module without compromising interconnection reliability or manufacturing throughput. It should be emphasized that the equivalent curing time introduced in this work serves as a semi-empirical interpretive metric for organizing experimental trends under non-isothermal conditions, rather than as a predictive curing-kinetics model.

The present study intentionally focuses on the formative stage of ECA interconnection, establishing clear relationships between processing conditions and initial electrical performance. Long-term reliability aspects, including performance stability under accelerated aging conditions such as damp heat (DH) and thermal cycling (TC), as well as quantitative contact resistivity extraction, were beyond the primary scope of this work. Nevertheless, DH and TC tests are currently in progress to evaluate the long-term stability of the proposed interconnection scheme, and the corresponding results will be reported in future work.

Overall, these results demonstrate that precise control of the thermal budget is essential for achieving low-resistance and mechanically stable interconnections in next-generation high-efficiency PV modules. The findings provide practical guidelines for optimizing ECA

curing processes and establish a solid foundation for scalable, low-thermal-budget manufacturing and subsequent reliability assessment of advanced HPBC module technologies.

Author Contributions: M.K.: Conceptualization, Methodology, Investigation, Formal analysis, Data curation, Validation, Visualization, Writing—original draft, Writing—review & editing. W.C.: Investigation, Validation, Formal analysis, Data curation, Writing—review & editing. G.K., K.J., J.S. (Jinyong Seok), J.S. (Jinho Shin): Investigation, Writing—review & editing. C.J.: Conceptualization, Funding acquisition, Project administration, Supervision, Writing—review & editing. All authors have read and agreed to the published version of the manuscript.

Funding: This work was partially supported by the Korea Institute of Energy Technology Evaluation and Planning (KETEP) through a grant funded by the Korean government (MOTIE) (RS-2023-00303745, titled "Development of photovoltaic module materials and process technology with low carbon emissions and easy recycling." Additional support was provided by the Korea Institute of Planning and Evaluation for Technology in Food, Agriculture and Forestry (IPET) and the Korea Smart Farm R&D Foundation (Kos-Farm) through the Smart Farm Innovation Technology Development Program, funded by the Ministry of Agriculture, Food and Rural Affairs (MAFRA) and the Ministry of Science and ICT (MSIT), Rural Development Administration (RDA) (RS-2025-02305965). This work was also supported by the Korea Institute of Industrial Technology (KITECH) under grant EH-26-0003, titled "Development of core technologies of AI based self-power generation and charging for next-generation mobility.".

Data Availability Statement: The original contributions presented in this study are included in the article. Further inquiries can be directed to the corresponding author.

Conflicts of Interest: The authors declare no conflict of interest.

References

1. Van Kerschaver, E.; Beaucarne, G. Back-contact solar cells: A review. *Prog. Photovolt. Res. Appl.* **2006**, *14*, 107–123. [CrossRef]
2. Kopecek, R.; Buchholz, F.; Mihailetchi, V.D.; Libal, J.; Lossen, J.; Chen, N.; Chu, H.; Peter, C.; Timofte, T.; Halm, A.; et al. Interdigitated Back Contact Technology as Final Evolution for Industrial Crystalline Single-Junction Silicon Solar Cell. *Solar* **2023**, *3*, 1–14. [CrossRef]
3. Mat Desa, M.K.; Sapeai, S.; Azhari, A.W.; Sopian, K.; Sulaiman, M.Y.; Amin, N.; Zaidi, S.H. Silicon back contact solar cell configuration: A pathway towards higher efficiency. *Renew. Sustain. Energy Rev.* **2016**, *60*, 1516–1532. [CrossRef]
4. Weber, J.; Roessler, T. How to assess the electrical quality of solar cell interconnection in shingle solar modules. *Prog. Photovolt. Res. Appl.* **2023**, *31*, 949–959. [CrossRef]
5. Wolf, M.; Rauschenbach, H. Series resistance effects on solar cell measurements. *Adv. Energy Convers.* **1963**, *3*, 455–479. [CrossRef]
6. Devoto Acevedo, M.I.; Wienands, K.; Halm, A.; Großer, S.; Gottschalg, R.; Tune, D. Influence of micro- and macrostructure when determining the contact resistivity of interconnects based on electrically conductive adhesives. *Sol. Energy Mater. Sol. Cells* **2023**, *260*, 112490. [CrossRef]
7. Sulas, D.B.; Johnston, S.; Jordan, D.C. Comparison of photovoltaic module luminescence imaging techniques: Assessing the influence of lateral currents in high-efficiency device structures. *Sol. Energy Mater. Sol. Cells* **2019**, *192*, 81–87. [CrossRef]
8. Shin, H.; Han, E.; Park, N.; Kim, D. Thermal Residual Stress Analysis of Soldering and Lamination Processes for Crystalline Silicon PV Modules. *Energies* **2018**, *11*, 3256. [CrossRef]
9. Beinert, A.J.; Romer, P.; Heinrich, M.; Aktaa, J.; Neuhaus, H. Thermomechanical design rules for photovoltaic modules. *Prog. Photovolt. Res. Appl.* **2023**, *31*, 1181–1193. [CrossRef]
10. Köntges, M.; Kurtz, S.; Packard, C.E.; Jahn, U.; Berger, K.; Kato, K.; Van Iseghem, M. *Review of Failures of Photovoltaic Modules*; IEA-PVPS T13-01:2014; International Energy Agency Photovoltaic Power Systems Programme: St. Ursen, Switzerland, 2014.
11. Rendler, L.C.; Beinert, A.J.; Walter, J.N.; Eitner, U. Thermomechanical stress in solar cells: Contact pad modeling and reliability analysis. *Sol. Energy Mater. Sol. Cells* **2019**, *196*, 167–177. [CrossRef]
12. Klasen, N.; Weber, J.; Beinert, A.J.; Eitner, U. Root cause analysis of solar cell cracks at shingle joints. *Sol. Energy Mater. Sol. Cells* **2022**, *238*, 111590. [CrossRef]
13. Sancaktar, E.; Bai, L. Electrically Conductive Epoxy Adhesives. *Polymers* **2011**, *3*, 427–466. [CrossRef]
14. Aradhana, R.; Mohanty, S.; Nayak, S.K. A review on epoxy-based electrically conductive adhesives. *Int. J. Adhes. Adhes.* **2020**, *99*, 102596. [CrossRef]

15. Kim, H.K.; Shi, F.G. Electrical reliability of electrically conductive adhesive joints: Dependence on curing condition and current density. *Microelectron. J.* **2001**, *32*, 315–321. [CrossRef]
16. Vyazovkin, S.; Burnham, A.K.; Criado, J.M.; Pérez-Maqueda, L.A.; Popescu, C.; Sbirrazzuoli, N. ICTAC kinetics committee recommendations for performing kinetic computations on thermal analysis data. *Thermochim. Acta* **2011**, *520*, 1–19. [CrossRef]
17. Kamal, M.R.; Sourour, S. Kinetics and thermal characterization of thermoset cure. *Polym. Eng. Sci.* **1973**, *13*, 59–64. [CrossRef]
18. Schulte-Huxel, H.; Blankemeyer, S.; Morlier, A.; Brendel, R.; Köntges, M. Interconnect-shingling: Maximizing the active module area with conventional module processes. *Sol. Energy Mater. Sol. Cells* **2019**, *200*, 109991. [CrossRef]
19. Jaubert, J.-N.; Nair, S.V.; Cai, J.; Lv, R.; Marteau, B.; Xu, T.; Zhang, G.; Ruda, H.E. Conductive adhesive based shingled solar cells: Electrical degradation under cyclic loading. *Sol. Energy* **2022**, *245*, 111823. [CrossRef]
20. Böck, L.; Rößler, T. Characterization of Electrically Conductive Adhesives to Enable Perovskite-Silicon Tandem Solar Cell Interconnection. In Proceedings of the SiliconPV 2024, 14th International Conference on Crystalline Silicon Photovoltaics, Chambéry, France, 15–19 April 2024; TIB Open Publishing: Hannover, Germany, 2024; Volume 2. [CrossRef]
21. Ronayette, N.; Poncelet, O.; Nobre, S.S.; Barthélémy, S.; Bellet, D.; Monna, R. Reduction of silver content in Electrically Conductive Adhesives for low-temperature interconnection of solar cells. *Sol. Energy Mater. Sol. Cells* **2025**, *292*, 113762. [CrossRef]
22. Perelman, A.; Barth, V.; Mandorlo, F.; Voroshazi, E. Critical materials and PV cells interconnection. *EPJ Photovolt.* **2024**, *15*, 4. [CrossRef]
23. Cui, H.W.; Wang, S.; Zhao, J.; Lin, J.X. Using Ozawa method to study the curing kinetics of electrically conductive adhesives. *J. Therm. Anal. Calorim.* **2014**, *117*, 1365–1373. [CrossRef]
24. Hartweg, B.; Fisher, K.; Niverty, S.; Chawla, N.; Holman, Z. Analysis of electrically conductive adhesives in shingled solar modules by X-ray imaging techniques. *Microelectron. Reliab.* **2022**, *136*, 114627. [CrossRef]
25. Acevedo, M.I.D.; Wells, R.; Großer, S.; Wienands, K.; Rudolph, D.; Halm, A.; Gottschalg, R.; Tune, D. The effects of increasing filler loading on the contact resistivity of interconnects based on silver–epoxied conductive adhesives and silver metallization pastes. *Prog. Photovolt. Res. Appl.* **2025**, *33*, 143–157. [CrossRef]
26. Chen, A.X.; Azpiroz, N.A.; Brew, S.E.; Valdez, A.M.; Esparza, G.L.; Qie, Y.; Valdez, N.J.; Blau, R.; Bunch, J.A.; Perry, T.J.; et al. Silver-free intrinsically conductive adhesives for shingled solar cells. *Cell Rep. Phys. Sci.* **2024**, *5*, 101967. [CrossRef]
27. Trupke, T.; Pink, E.; Bardos, R.A.; Abbott, M.D. Spatially resolved series resistance of silicon solar cells obtained from luminescence imaging. *Appl. Phys. Lett.* **2007**, *90*, 093506. [CrossRef]
28. Hinken, D.; Ramspeck, K.; Bothe, K.; Fischer, B.; Brendel, R. Series resistance imaging of solar cells by voltage dependent electroluminescence. *Appl. Phys. Lett.* **2007**, *91*, 182104. [CrossRef]
29. Trupke, T.; Mitchell, B.; Weber, J.w.; McMillan, W.; Bardos, R.A.; Kroeze, R. Photoluminescence imaging for photovoltaic applications. *Energy Procedia* **2012**, *15*, 135–146. [CrossRef]
30. Colvin, D.J.; Schneller, E.J.; Davis, K.O. Cell dark current–voltage from non-calibrated module electroluminescence images. *Solar Energy* **2022**, *244*, 448–456. [CrossRef]
31. Jordan, D.C.; Kurtz, S.R. Photovoltaic degradation rates—An analytical review. *Prog. Photovolt. Res. Appl.* **2013**, *21*, 12–29. [CrossRef]
32. Fukushima, T.; Inoue, M. Control of Silver Micro-Flakes Sintering and Connection Properties of Epoxy-Based Conductive Adhesives. *Materials* **2025**, *18*, 217. [CrossRef]
33. Acevedo, M.I.D.; Wienands, K.; Halm, A.; Gottschalg, R.; Tune, D. Environmental Stability of the Contact Resistivity of Interconnects Based on ECAs. *IEEJ Trans. Electr. Electron. Eng.* **2025**, *20*, 2056–2072. [CrossRef]
34. Rißland, S.; Breitenstein, O. Evaluation of luminescence images of solar cells for injection-level dependent lifetimes. *Sol. Energy Mater. Sol. Cells* **2013**, *111*, 112–114. [CrossRef]

Disclaimer/Publisher's Note: The statements, opinions and data contained in all publications are solely those of the individual author(s) and contributor(s) and not of MDPI and/or the editor(s). MDPI and/or the editor(s) disclaim responsibility for any injury to people or property resulting from any ideas, methods, instructions or products referred to in the content.